



SUSTAINABLE METHYLENE BLUE REMOVAL USING ROSEMARY-DERIVED ACTIVATED CARBON AND GREEN NANOPARTICLES

BERAFTA M.¹, KHELILI H.^{1}, GUELLAL M.¹,
ACHOUR S.², KONANK.G.³*

¹ Laboratory of Processes Engineerin Chemical, Ferhat Abbas,
University of Setif 1, 19000 Setif, Algeria

² Professor, Research laboratory in subterranean and surface hydraulics (LARHYSS),
University of Biskra, Algeria

³ Doctor, Environmental Sciences Laboratory_Nangui Abrogoua, University 02 BP 801
Abidjan 02, Abidjan, Ivory Coast

(*) *khelili.hinda@yahoo.fr*

Research Article – Available at <http://larhyss.net/ojs/index.php/larhyss/index>
Received September 22, 2024, Received in revised form March 23, 2025, Accepted March 25, 2025

ABSTRACT

The study aimed to assess the efficiency of methylene blue (MB) dye removal from wastewater using two sustainable and cost-effective adsorbents derived from rosemary: activated rosemary carbon (AR) and iron-polyphenol nanoparticles (Fe-P). AR was produced through phosphoric acid activation of rosemary waste, while Fe-P was synthesized using green nanotechnology with rosemary extract and an iron precursor. Characterization techniques such as FTIR, SEM, and XRD revealed that AR had an amorphous structure with a well-developed pore network, while Fe-P exhibited a crystalline structure with highly reactive nanoparticles. Adsorption experiments showed optimal MB removal at pH 7.5 for AR and in more acidic conditions for Fe-P, with AR achieving a higher maximum adsorption capacity (894.81 mg/g) compared to Fe-P (603.96 mg/g), as modeled by the Langmuir isotherm. The pseudo- second -order kinetic model best described the adsorption process, indicating surface adsorption as the dominant mechanism, with Fe-P showing faster adsorption rates. Thermodynamic analysis confirmed the adsorption process was spontaneous and exothermic, favoring lower temperatures. Regeneration studies demonstrated AR's superior reusability, maintaining efficiency over multiple cycles. Overall, the results highlight the potential of AR and Fe-P as eco-friendly solutions for industrial dye pollution, combining sustainability with high performance.

Keywords: Adsorption, Methylene blue, Rosemary, Nanoparticles, Wastewater.

INTRODUCTION

The proliferation of dye-containing industrial waste has become a critical environmental concern. Recent studies investigate the use of dry spearmint sprigs as a low-cost, eco-friendly biosorbent for removing methyl violet 10B dye from aqueous solutions. The research highlights the adsorbent's high removal efficiency and potential for sustainable wastewater treatment applications (Boudaoud et al., 2024). Furthermore, many authors explored the adsorption capacity of biosorbents prepared from mango seed kernels for the removal of methyl orange dye from aqueous solutions, emphasizing the effectiveness of using agricultural waste materials in dye wastewater treatment (Khelifi et al., 2018). A previously conducted, highly pertinent study assessed the efficacy of biosorbents derived from Algerian date stones in adsorbing methylene blue dye from aqueous solutions, highlighting the potential of utilizing local agricultural by-products in wastewater treatment processes (Khelifi et al., 2016). These articles contribute valuable insights into sustainable and cost-effective methods for treating dye-laden industrial wastewater, addressing a critical environmental concern.

Dyes as pollutants are particularly problematic because their chemical stability, while beneficial for their intended use, makes them extremely difficult to remove from wastewater. Environmental agencies worldwide have recognized this challenge, as these compounds not only disrupt aquatic ecosystems but also pose significant risks to human health (Hamzade et al., 2022). Colours are widely used across industries like rubber, textile, cosmetics, leather, fuel, pharmaceuticals, and food, which employ various dyes to manufacture diverse products. It is estimated that around 7×10^5 tons of dyes and pigments are consumed worldwide annually (Gupta et al., 2013), with nearly 100 tons/year released into wastewater (Dizge et al., 2008). As a result, substantial coloured effluent from these industries is discharged into the natural environment. Their presence in water bodies poses serious risks to both humans and aquatic life (Khelili et al., 2024).

Dyes can modify the colour characteristics of different products in various industries. They are typically defined as ionized and aromatic organic compounds (Yagub et al., 2014). Dyes can be broadly classified into anionic, cationic, and non-ionic types. Even at very low concentrations, dyes present serious pollution threats owing to their intense toxicity and high persistence in the environment (Nghah et al., 2011; Hameed et al., 2013). Moreover, the chemicals in dyes and degraded dyes found in dye-containing wastewater are typically poisonous or even mutagenic, carcinogenic, causing major harm to humans and aquatic life. For example, when dye-laden wastewater enters aquatic ecosystems, the toxic pollutants tend to accumulate in some fish tissues. Ultimately, these harmful substances may enter the human body through the food chain, resulting in many pathological issues (Afroze et al., 2018). Due to the large amounts and impacts, removing these pollutants is a major concern. Many physical, chemical, and biological treatment technologies (trickling filters, activated sludge, chemical coagulation, ion exchange, precipitation, carbon adsorption, and processes) have been extensively studied for eliminating dyes from wastewater effluents (Fadhil et al., 2019; Urooj et al., 2024).

The adsorption method, which is of crucial interest in this study, has consistently demonstrated high efficiency in water treatment, effectively removing a wide range of pollutants, including heavy metals, dyes, organic compounds, and emerging contaminants from aqueous solutions (Bouchemal and Achour, 2007; Ouakouak et al., 2010; Khelili et al., 2010; Ouakouak and Youcef, 2016; Mumthaj et al., 2023). Owing to its simplicity, cost-effectiveness, and high removal capacity, the adsorption method has been widely adopted and continuously developed in the water treatment field from the early 20th century to the present (Benzizoune et al., 2004; Yeddou et al., 2012; Guergazi et al., 2013; Youcef et al., 2014).

Moreover, as a versatile water treatment technique, adsorption has been successfully applied to treat industrial effluents, municipal wastewater, and groundwater, making it one of the most adaptable methods in the field (Ounoki and Achour, 2014; Kheliel et al., 2014; Gaouar and Gaouar, 2016; Masmoudi et al., 2018; Yadav et al., 2024).

The adsorption method is preferred for removing dyes from industrial effluents over other techniques since it is efficient, cost-effective, and reusable. Researchers are also closely pursuing adsorption as a viable approach for eliminating dyes from wastewater due to its simplicity of fabrication, sensitivity to pollutants, and potential for industrial-scale application. To enhance adsorption efficiency, adsorbents have been continuously modified regarding pore structure and surface chemistry (Awang Nasrizal et al., 2023). The use of adsorbents derived from biomass sources to remove dyes has recently garnered much interest owing to their renewable nature, low cost, and abundance (Abba et al., 2019; Chauhan and Dikshit, 2023; Song et al., 2023). Nanotechnology involves the synthesis of nanoparticles with varying sizes, shapes, and chemical compositions that can have immense potential applications in diverse fields (Anandan et al., 2023). Metal nanoparticles, such as iron nanoparticles (Fe-P), have been found to possess wide functionality for purposes like wastewater treatment (Zhang et al., 2011). Metal nanoparticles with desired properties like size and shape are typically synthesized using various physical and chemical processes with major drawbacks like high cost (Narayanan et al., 2010; Gan et al., 2012). Therefore, there is a clear need for a willing, cost-effective, safe, and biocompatible system for nanoparticle production (Raveendran et al., 2003; Shah et al., 2014).

Activated carbon is renowned for its exceptional adsorption capabilities, making it a pivotal component in water and wastewater treatment processes. Its porous structure and extensive surface area enable the effective removal of a wide range of contaminants, including organic compounds, dyes, heavy metals, and other pollutants. Activated carbon can be derived from a wide range of natural and synthetic materials, with agricultural waste products such as coconut shells, rice husks, and orange peels being some of the most sustainable and cost-effective sources. Industrial by-products, including paper mill sludge, bagasse, and spent tea grains, offer an economical alternative for activated carbon production, transforming waste into valuable adsorbents. Coal-based activated carbon, derived from bituminous, sub-bituminous, and lignite coal, remains one of the most widely used forms of activated carbon due to its high adsorption capacity and availability. Activated carbon derived from lignite and peat is particularly effective for removing colour, taste, and odor from drinking water, making it a popular choice in municipal water

treatment facilities. The following relevant references provide the keys to all aspects previously mentioned (Pelekani and Snoeyink, 1999; Knappe, 2006; Xia and Shi, 2016; Zieliński et al., 2022).

The primary objective of this study is to evaluate the effectiveness of rosemary-derived adsorbents activated rosemary carbon (AR) and iron-polyphenol nanoparticles (Fe-P) in removing methylene blue (MB) dye from wastewater. This work aimed to harness renewable agricultural waste and green synthesis methods to create cost-effective and environmentally friendly solutions for dye pollution. To achieve this, the study involves several key stages: preparation and characterization of AR and Fe-P, optimization of adsorption parameters such as pH, adsorbent dosage, and contact time, and analysis of adsorption kinetics and isotherms to elucidate the adsorption mechanisms. Thermodynamic studies are conducted to assess the feasibility and spontaneity of the adsorption process, while the reusability of the adsorbents is evaluated through regeneration cycles. By combining renewable resources and green nanotechnology, this work contributes to the development of innovative and sustainable materials for water treatment.

MATERIAL AND METHODS

Chemicals

The rosemary waste used in this study was sourced from a garden in El-Eulma, a city in northeastern Algeria. Other chemicals employed included phosphoric acid (H_3PO_4 , 85%), iron (III) chloride hexahydrate ($FeCl_3 \cdot 6H_2O$), sodium hydroxide (NaOH, 98%), and hydrogen chloride (HCl, 37%).

The solvent used in this study was wastewater sourced from Oued Bouslam, located in the city of Setif, Algeria.

The main characteristics of the model dye, methylene blue (MB), are compiled in Table.1.

Table 1: Essential Characteristics of Methylene Blue (Kordkandi et al., 2014).

Methylene blue dye (MB)	
Category	Basic cationic dye
Brute formula	$C_{16}H_{18}N_3SCl$
Chemical name	Tetra methylthionine hydrochloride
Molar mass (g/mol)	320
C.I. number	52.015
Maximum wavelength (nm)	664
pKa	3.8

Preparation of the adsorbents

Rosemary is a relatively drought-tolerant plant used in landscaping for hedges and rock gardens, especially during spring. After spring, the rosemary hedges are often burned or discarded, making this plant a potential waste resource for contaminant removal. The rosemary waste was collected, rinsed, dried overnight at 80°C, and crushed into powder (R). The powder was mixed with (6 M) phosphoric acid (H₃PO₄, 85%) in a (1:2) weight-to-volume ratio. The mixture was left under stirring for 24 hours, which was washed with water until the pH reached 6.5. Finally, the mixture was dried, producing an activated rosemary material (AR).

Aqueous rosemary extract was prepared by boiling 50 g of crushed leaves in 250 ml of distilled water at 80 °C Celsius for 1 h. The mixture was allowed to settle for 1 h (Wang et al., 2013), then vacuum filtered and stored at 4°C Celsius for later use. (Iron nanoparticles were synthesized using iron (III) chloride hexahydrate (FeCl₃·6H₂O) as the iron precursor. A (0.10 M) solution of FeCl₃ was made by dissolving 1.62 g of FeCl₃ in 100 ml of distilled water (Zhiqiang et al., 2014). The 0.10 M FeCl₃ solution was then added to the rosemary extract in a (2:1) volume ratio and heated at 80°C Celsius for 1 h with constant stirring at 540 rpm. This resulted in a black-colored solution with a pH of 4.40. After nanoparticle synthesis, (0.5 M) sodium hydroxide (NaOH) was incrementally introduced to the black iron nanoparticle solution, altering the pH from 4.40 to 11. Despite the significant pH change, the solution persisted as a black colloid. The iron nanoparticle suspension was then agitated for 2h. The final black nanoparticle dispersion was dehydrated in a 100°C oven for 17 hours. A Fe-Polyphenol molecule structure is illustrated in (Fig. 1).

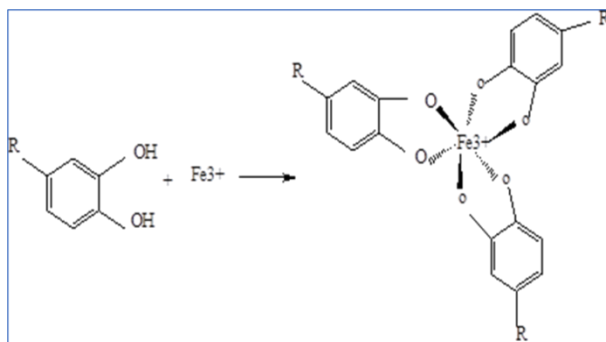


Figure 1: Proposed molecular structure of Fe–Polyphenol material (Aichour et al., 2018)

Adsorption study

The amount of dye adsorption was determined using Eq. (1), and the removal efficiency of MB (%) was determined by using the following Eq. (2). Several parameters that can

impact the adsorption of methylene blue on the adsorbents were evaluated, such as initial pH, adsorbent dose, and contact time.

$$Q_e = (C_0 - C_e) \times V/m \quad (1)$$

$$R(\%) = (C_0 - C_e/C_e) \times 100 \quad (2)$$

C_0 represents the initial concentration of MB in mg/L, C_e represents the equilibrium concentration of MB in (mg/L), V denotes the volume of the solution being treated in L, and m denotes the mass of the adsorbents employed in g.

The residual concentrations of MB were measured using a Shimadzu Spectrophotometer UV-1700UV at the maximum absorbance wavelength of 664 nm.

Effect of Adsorbent Dose

To study the capacity to remove a dye from the solution, several doses of the adsorbents AR, and Fe-P, from 50 mg/L to 1000 mg/L are studied. To identify the ideal dosages, 10 mL aliquots of a 10 mg/L MB dye solution prepared from wastewater were interacted with increasing quantities of the different adsorbents. The solutions were agitated at room temperature at 200 rpm /24 h, at the initial pH of 7.5 without adjustment. After reaching equilibrium, the solutions were permitted to settle before collecting the supernatants for dye concentration analysis visible UV. Removal of the MB dye by the adsorbents was evaluated at each dosage amount. The ideal dosage for the maximum binding and retention of the contaminant dye was determined.

Initial pH effect

The initial pH is one of the most critical environmental variables affecting adsorption efficiency, as it impacts contaminant solubility, sorbent surface charge, and pollutant ionization state. To explore how pH influences MB binding onto the adsorbents AR, and Fe-P, adsorption experiments were conducted over a wide pH range from 2.0 to 11.0. Using 10 mL aliquots of a 10 mg/L MB dye solution prepared in simulated wastewater, the effects of initial pH were investigated while holding other conditions constant (contact time: 24 hours, temperature of room, dosages: 4 mg AR, 4 mg Fe-P).

Kinetics of adsorption

A batch system was used to investigate methylene blue (MB) adsorption kinetics on AR, and Fe-P at room temperature (20 °C). The goal was to assess how the adsorbed quantity varied with time and initial dye concentration. Four MB solutions were prepared, with initial concentrations ranging from 3 to 20 mg/L. The adsorbent amounts used were 400 mg/L of AR, and 400 mg/L of Fe-P composite. A pH of 7.5 and a mixing speed of 250 rpm were maintained throughout the experiments. Samples were collected at well-defined intervals and analyzed using a visible UV.

To elucidate the adsorption mechanism, five models were employed: the pseudo-first-order Eq. (3), the pseudo-second-order Eq. (4), and the Elovich Eq. (5) models, as well as the intra-particle diffusion Eq. (6).

$$Q_t = Q_e(1 - e^{-K_1 t}) \quad (3)$$

$$Q_t = K_2 Q_e^2 t / 1 + K_2 Q_e t \quad (4)$$

$$Q_t = \frac{1}{B} \ln(ABt + 1) \quad (5)$$

$$Q_t = K_{int} t^{1/2} + C \quad (6)$$

$$E_r = \frac{1}{n} \sum_{i=1}^n \frac{q_{e,i}^{mod} - q_{e,i}^{exp}}{q_{e,i}^{exp}} \quad (7)$$

K_1 (min^{-1}) represents the rate constant for the pseudo-first-order (PFO) model, k_2 ($\text{g/mg} \cdot \text{min}$) represents the rate constant for the pseudo-second-order (PSO) model, C (mg/g) denotes the constant associated with the boundary layer thickness, A is the initial adsorption rate constant ($\text{mg/g} \cdot \text{min}$), B the desorption constant related to surface coverage and activation energy (g/mg), K_{int} [$\text{mg}/(\text{g} \times \text{min}^{1/2})$] represents the rate constant of the Weber-Morris model. The pseudo-first-order (PFO) model, also known as the mass transfer model was the first employed to describe the adsorption kinetics of MB onto the adsorbents (Magdy et al., 2018). The pseudo-second-order (PSO) model, which is based on chemisorption, was also applied (Magdy et al., 2018; Stanciu et al., 2018). Furthermore, the intra-particle diffusion models were used to describe the diffusion of MB within the porous structures of the two adsorbents, The parameter n represents the total number of data points collected during the experiment, The term $q_{e,i}^{mod}$ refers to the modeled adsorption capacity corresponding to data point i , On the other hand, $q_{e,i}^{exp}$ denotes the experimental adsorption capacity obtained from laboratory measurements for the same data point i .

Effects of Temperature

The impact of temperature on adsorption characteristics was investigated by conducting experiments at 20°C, 30°C, and 40°C. Adsorption isotherms were obtained by varying the initial concentrations from 3 to 400 mg/L under a rotation speed of 200 rpm. The equilibrium times and doses for the different adsorbents were as follows: 30 min and 400 mg/L for AR, and 20 min and 400 mg/L for Fe-P. A analysis visible UV was employed to measure the initial and final concentrations of the MB dye. The adsorbed quantities were calculated using the relationship given in Eq. (1). Classical isotherm models, namely the Langmuir Eq. (8), Freundlich Eq. (9), Redlich-Peterson models Eq. (10), and Langmuir-Freundlich Eq. (11), were proposed to correlate the experimental data.

$$Q_e = Q_{max} K_L C_e / 1 + K_L C_e \quad (8)$$

$$Q_e = K_f C_e^{1/n} \quad (9)$$

$$Q_e = KC_e/1 + \alpha C_e^\beta \quad (10)$$

$$Q_e = Q_s(bC_e)^n/1 + (bC_e)^n \quad (11)$$

In the Langmuir model, Q_{max} (mg/g) represents the maximum adsorption capacity, while K_L (L/mg) is the Langmuir constant. For the Freundlich model, $K_f[(mg/g)/(L/mg)^{1/n}]$ and n (dimensionless) are the characteristic constants. The Redlich-Peterson model employs K (L/g) and α (mg/L) $^{-\beta}$ as isotherm constants, with β the dimensionless exponent constrained between 0 and 1. In the Langmuir-Freundlich model, Q_s (mg/g) denotes the maximum adsorption capacity, b (L/mg) is the equilibrium constant, and n characterizes the surface heterogeneity of the adsorbent.

Study of AR regeneration

The reusability of pinecone-derived AR was evaluated through multiple adsorption cycles. In each cycle, 300 mg of adsorbent was dispersed in 300 mL of MB solution (100 mg/L), and the adsorption test was conducted under optimized kinetic conditions with a fixed equilibrium time of 40 min. After each adsorption cycle, the AR was recovered by filtration, dried, and reused for subsequent adsorption tests. The cycling process was continued until the removal efficiency dropped below 50%. For regeneration studies, the spent adsorbent from the final cycle was treated with 0.1 M HCl solution under stirring for 3 hours, followed by thorough washing with distilled water. The regenerated adsorbent was then subjected to fresh adsorption tests, and the removal efficiency was calculated.

Materials characterization

The surface chemistry of AR, and Fe-P was examined using an Agilent Technologies Fourier Transform Infrared (FTIR) Spectrophotometer (Cary 600 series FTIR spectrometer). The infrared spectra were recorded from 4000 cm^{-1} to 500 cm^{-1} .

The micromorphology of AR, and Fe-P composite was examined using scanning electron spectroscopy (SEM). The SEM images were captured using a Quanta 250 instrument. Additionally, elemental analysis was conducted on the same apparatus using energy-dispersive X-ray diffraction (EDX). The adsorbents' crystalline nature and structural properties were analyzed using an X-ray diffraction technique (XRD). The thermal stability of the prepared materials was investigated using thermogravimetric analysis (TGA), The measurements were performed on an SDT Q600 V20.9 Build 20 instrument. Samples were heated from 25°C to 1000°C at a constant heating rate of 10°C / min under controlled atmospheric conditions.

The zero-charge point (pH_{pzc}) for each material, corresponding to a zero-charge potential on the adsorbent surface, was determined. This parameter is crucial for understanding the interaction mechanism between the liquid and solid phases. A simple protocol was followed: a series of 6 beakers containing 20 mg of adsorbent and 20 mL of distilled water was prepared. The initial pH of the water was adjusted from 2 to 11 using HCl or NaOH.

These suspensions were kept under stirring for 48 hours, and then the final pH of each beaker was measured. Finally, the results were displayed on a graph using the expression $\Delta pH = f(pH_i)$.

RESULTS AND DISCUSSION

Characterization of the materials

The FTIR spectra unveil the presence of various functional groups and molecular vibrations within the AR, and Fe-P samples (Fig. 2). A broad absorption band centered around 3425 cm^{-1} is observed, which can be ascribed to the stretching vibrations of O-H, N-H, and C-O-H moieties present on the surface of the materials, corroborating findings from related literature (Tiwari et al., 2017).

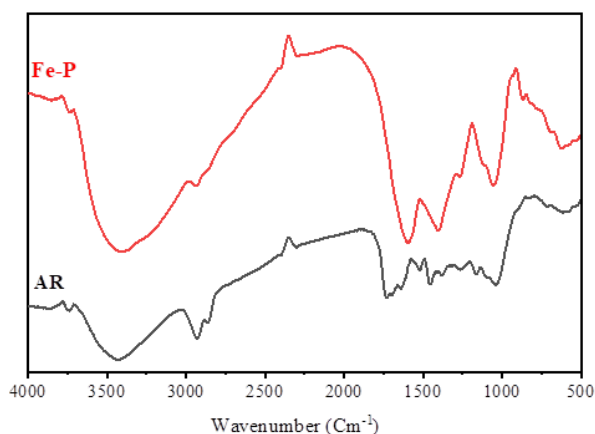


Figure 2: Fourier-Transform Infrared spectroscopy profiles of AR and Fe-P

Relatively weak bands at 2853 and 2923 cm^{-1} correspond to the vibrations of CH_2 and CH_3 groups, and symmetric stretching modes of carboxylate (C-O) groups. The absorption at 1258 cm^{-1} is attributed to C-O stretching vibrations. Furthermore, (Fig. 2) exhibits the presence of $\text{C}\equiv\text{N}$ moieties, aromatic C-H bonds, and certain phosphorus-containing compounds, as evidenced by the existence of peaks in the range of 1267 to 700 cm^{-1} (Nahil et al., 2012). The bands at 609 cm^{-1} and 597 cm^{-1} in the Fe-P sample is associated with iron oxide (Fe-O) vibrations (Sarala et al., 2020).

The micromorphology of AR, and Fe-P were examined using scanning electron microscopy, as shown in Fig. 3a and 3b. The images of AR reveal an irregular and heterogeneous surface morphology, with developed and fragmented pore structures of varying sizes. By fitting the histogram data, the average pore size was found to peak at $0.71\mu\text{m}$ (Fig. 4). However, the micrographs also show that the outer surface of the AR exhibits cracks and crevices (Naboulsi et al., 2023).

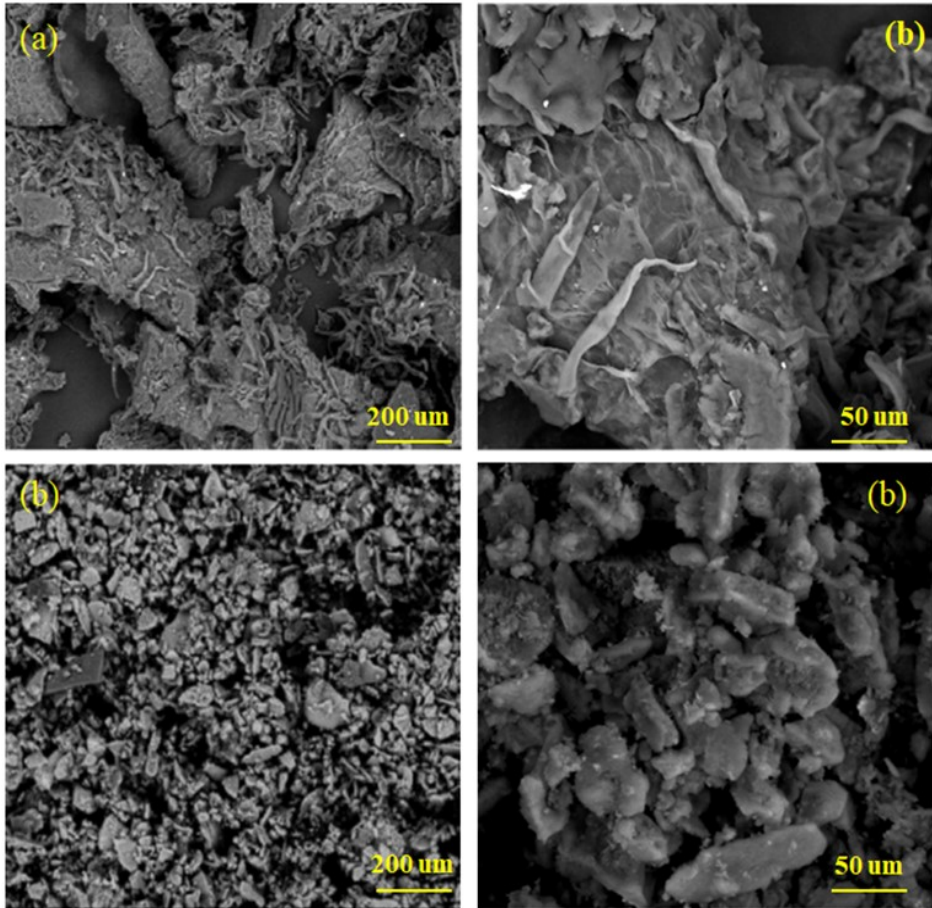


Figure 3: SEM captures of (a) AR, and (b) Fe-P

The surface morphology of the Fe-P displays highly agglomerated and self-assembled grains. Fitting the histogram with a Gaussian distribution gives an average yield of an average particle size that peaked at 49.401, as illustrated in (Fig. 4).

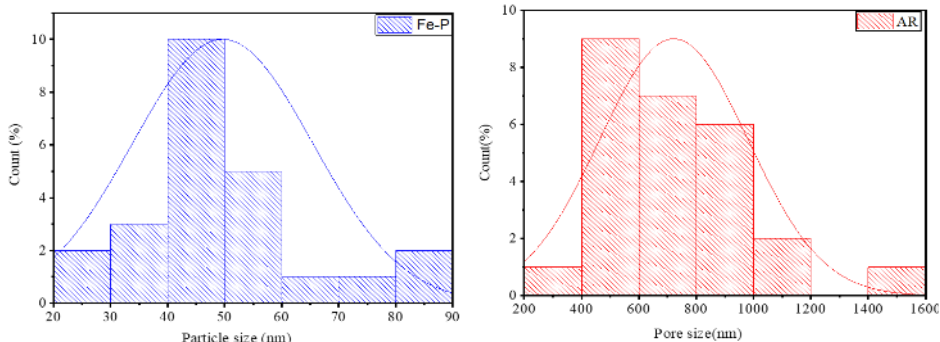


Figure 4: The average diameter of particles (Fe-P) and the pore (AR)

Elemental analysis of the AR, and Fe-P was conducted using energy-dispersive X-ray (EDX) spectroscopy, as shown in Fig. 5a and 5b. The elemental analysis of AR revealed that C and O are the dominant elements, with traces of Ca, Al, and Cl also present. For the Fe-P, the main elements identified were C (29.37 wt %), iron (11.79 wt %), and O (40.22 wt %). Compared to the AR, the Fe-P had a lower carbon content but contained more trace elements such as Mg, Al, Si, P, S, Na, K, Cl, and Ca. Adding NaOH (11.79 wt%), and O (40.22 wt%). Compared to the AR, the Fe-P had a lower carbon content but contained more trace elements such as Mg, Al, Si, P, S, Na, K, Cl, and Ca. Adding NaOH may have played a role in immobilizing these elements within the carbon framework, and the results were similar to those reported in the literature (Hung et al., 2023).

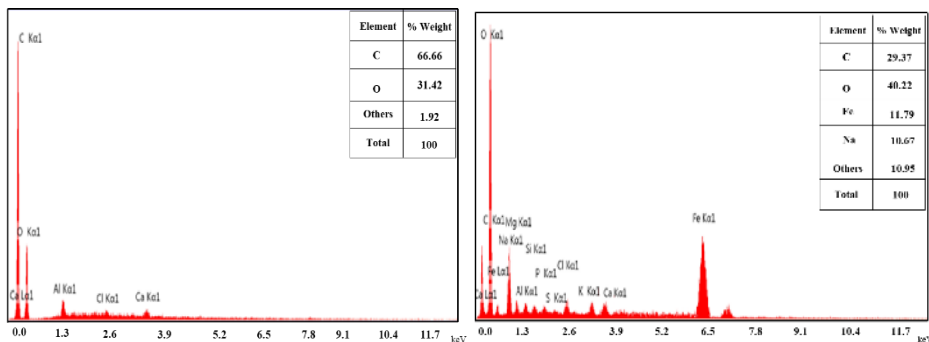


Figure 5: EDX spectra and XRF for adsorbents AR, and Fe-P

X-ray diffraction (XRD) analysis was performed to investigate the crystallinity of the AR, and Fe-P. The XRD pattern of AR, shown in Fig. 6a, does not exhibit any distinct sharp peaks, indicating a predominantly amorphous structure. This is evidenced by the high background signal spanning approximately 10-20 degrees. Additionally, two broad peaks are observed within the angular regions of approximately 20-30 degrees and 35-50 degrees. These broad peaks are characteristic of the disordered stacking of carbon rings in amorphous carbon materials. The largely amorphous structure is advantageous for activated carbons intended for use as microporous adsorbents, as it facilitates the formation of uniform micropores for efficient adsorption (Naboulsi et al., 2023). In

contrast, The XRD pattern of the Fe-P shown in Fig. 6b indicates the presence of several high-intensity, narrow diffraction peaks, revealing a highly crystalline structure. The peaks at $2\theta = 17.76, 28.2, 31.53, 35.01, 40.38, 45.42, 50.01, 56.28,$ and 66.27 corresponding to the reference pattern (JCPDS 014-0998). The average size of the iron nanoparticles (Fe-P) was estimated using the Debye-Scherrer equation Eq. (12), which relates the width of the X-ray diffraction (XRD) peaks to the size of the crystallites. This calculation yielded an average Fe-P size of 47.9689 nm. This result is consistent with the findings from the histogram analysis of the Fe-P (Fig. 4)

$$D = K\lambda/\beta \cos \theta \tag{12}$$

D represents the crystallite diameter size, λ denotes the wavelength of the radiation used, β symbolizes the full width at half-maximum (FWHM) intensity in radians, K represents a dimensionless shape factor with a value of 0.9 , θ signifies the diffraction angle in degrees.

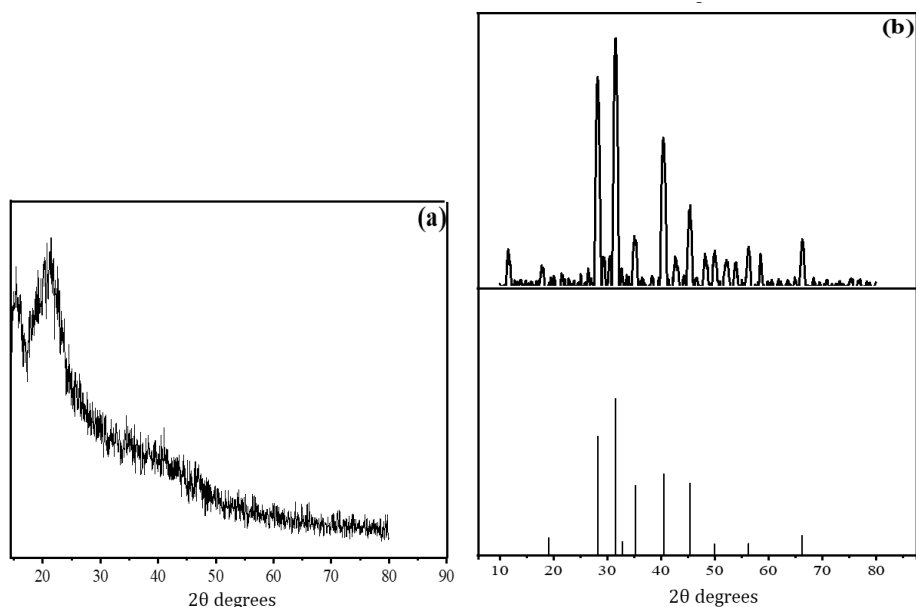


Figure 6: X-ray Diffraction (XRD) patterns of (a) AR and (b) Fe-P

Thermogravimetric analysis was carried out on AR, and Fe-P samples across a temperature range of 25 to 1000 °C, with the experimental data illustrated in (Fig. 7). The thermal decomposition profile revealed three distinct stages: initially, from 25 °C to 200 °C, the samples experienced weight losses of 4.43% for AR, and 19.84% for Fe-P, primarily attributable to the removal of adsorbed water and surface-bound volatile matter. The second stage, spanning 200 °C to 498 °C for AR and Fe-P, demonstrated significant mass reductions of 77.7% for AR, and 40% for Fe-P, which resulted from the decomposition of cellulosic elements. The final stage involved the gradual degradation of lignin, a component characterized by exceptional thermal stability compared to cellulose

and hemicellulose polymers, progressively decomposing until reaching a stable residual mass (Yudha et al., 2019).

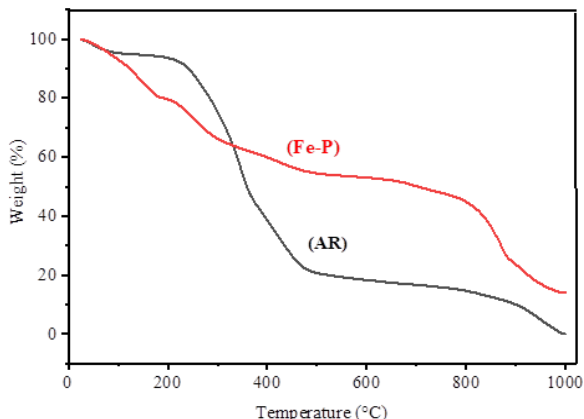


Figure 7: Thermogravimetric Analysis of AR and Fe-P

The zero-point of charge (pH_{pzc}) values for the AR, and Fe-P, composite was determined and are shown in (Fig. 8).

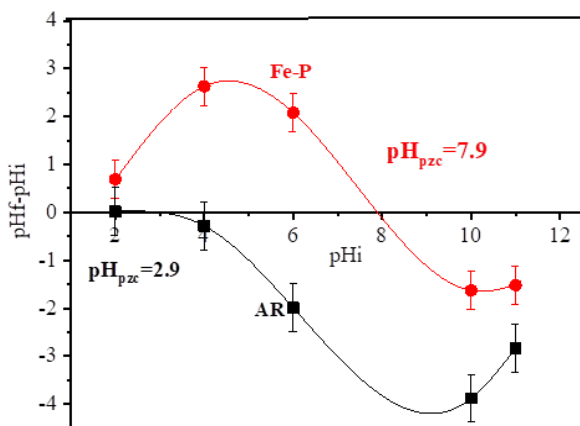


Figure 8: Isoelectric points of AR, and Fe-P. (T = 20 °C, stirring speed = 250 rpm)

The pH_{pzc} values were found to be 2.9, and 7.9, respectively. This information provides insights into the surface charge characteristics of the adsorbents. When the pH of the solution is below the pH_{pzc} value, the surface functional groups of the adsorbents are protonated by an excess of H^+ ions. Conversely, when the solution pH is greater than the pH_{pzc} value, the surface functional groups of the adsorbents are deprotonated by the excess of OH^- ions.

Effect of adsorbent dose

Fig. 9 plots the equilibrium adsorption capacity (mg/g) and percent dye removal against the adsorbent dosage (mg/L) for AR, and Fe-P. As the dosage increased from 50 to 1000 mg/L, the adsorption density substantially decreased from 162.5 to 9.3 mg/g for AR, and 157.3 to 8.4 mg/g for Fe-P. This decline stems from the dilutive effect of higher sorbent levels on the dye concentration gradient, reducing the driving force for mass transfer onto each adsorbent binding site (Shukla et al., 2002; Al-Ghouti et al., 2009). Conversely, the percentage of dye elimination rose with increasing dosage, from 81.2% to 93% for AR, and 78.6% to 84.3% for Fe-P over the same range.

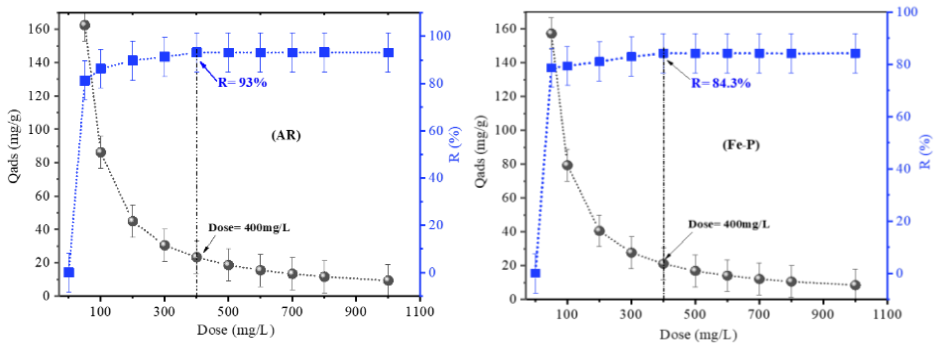


Figure 9: Effect of AR, and Fe-P, mass on the amount of adsorption and percent removal of MB. (T = 20 °C, stirring speed =250 rpm, pH = 7.5)

Initial pH effect

The results graphed in (Fig. 10) demonstrate the impact of initial pH on removing the MB.

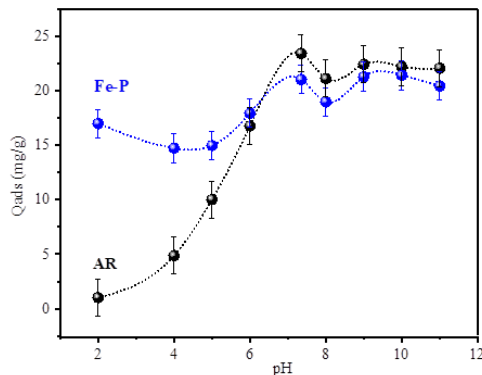


Figure 10: Influence of pH on the adsorption of MB onto AR, and Fe-P. (T= 20°C and stirring speed 250 rpm)

The results revealed that the two adsorbents exhibited effective adsorption in the unamended medium (pH=7.5), with AR adsorbing 23.4 mg/g, and Fe-P adsorbing 21 mg/g. It was observed that the adsorption increased in the basic medium for AR, while it decreased in the acidic medium. This behavior can be explained by considering the pH_{pzc} values (2.9 for AR). When the pH increases towards alkaline values, the availability of OH⁻ anions facilitates the adsorption of MB through electrostatic interactions. Conversely, as the pH decreases towards acidic values, the opposite effect occurs. Interestingly, for Fe-P, effective adsorption of 16.96 mg/g was observed in the acidic medium, despite having a positive surface charge similar to MB. This suggests that electrostatic interactions are not the sole mode of adsorption involved in the adsorption of MB onto Fe-P.

Kinetics of MB adsorption

Impact of the MB initial concentration and the contact time

The adsorption kinetic data graphed in (Fig. 11) for (AR), and (Fe-P) respectively demonstrate distinct multi-stage binding behaviors. Initial rapid dye uptake was observed within the first 40 min for AR, and 20 min for Fe-P as the MB molecules quickly diffused to occupy the readily accessible external surface sites. Subsequent adsorption proceeded at a slower rate as the remaining dye molecules had to penetrate deeper into pores and diffuse through boundary layer films to interact with the fewer uncovered internal binding sites. Final equilibration was achieved once all sites were saturated. Equilibrium adsorption capacities rose from 9.7 to 45.2 mg/g for AR, and 6.8 to 45 mg/g for Fe-P as initial dye concentrations increased from 5 to 20 mg/L. It is due to the driving force that increases with the initial concentration.

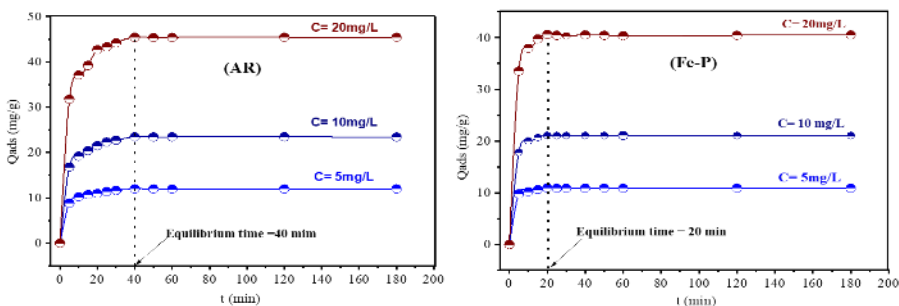


Figure 11: Effect of MB concentration on the adsorption capacity of AR, and Fe-P (pH 7.5, 400 mg/L for AR and Fe-P)

Modeling of kinetics

Fig. 12 and Table 2 present the results of modeling three models. A comparison between the experimental adsorbed quantities and the theoretical values obtained from each revealed that the PSO model was the most suitable for describing the adsorption kinetics

of MB onto AR, and Fe-P, outperforming the PFO and Elovich models. According to the literature, the pseudo-second-order kinetic model operates on the assumption that the rate-limiting step is chemical adsorption, involving the transfer of electrons between the adsorbent and the adsorbate (Sahnoun et al., 2018).

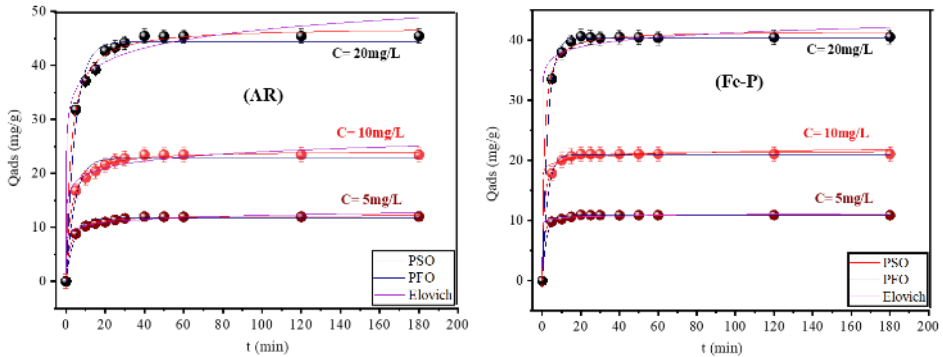


Figure 12: PFO, PSO, and Elovich Kinetics model of MB adsorption onto AR, and Fe-P

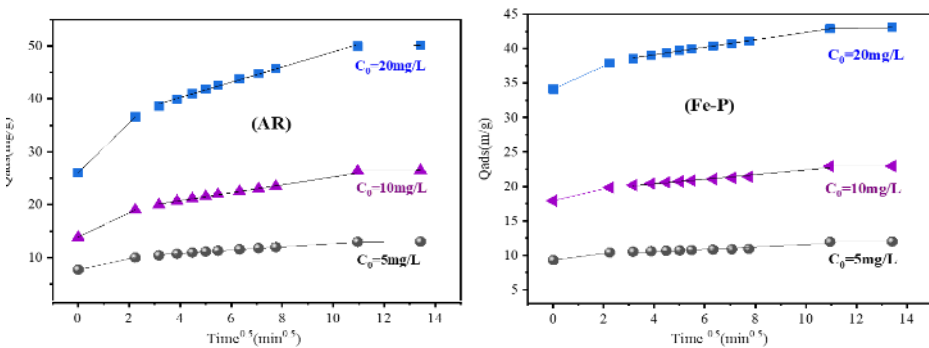


Figure 13: Modeling of intraparticle diffusion of MB adsorption onto AR, Fe-P

Fig. 13 depicts the intra-particle modeling curves. Regardless of the initial concentration, materials (AR, and Fe-P) exhibited multiline curves, indicating that the adsorption of MB occurred in three distinct stages. These stages can be characterized as follows: MB particles diffuse from the boundary of a layer to the external surface of the adsorbents, and this is called the first step. Then the MB particles are transferred from the outer surface to the inner layer of the adsorbents, and this is what we observe in the second stage. As for the third stage, equilibrium begins to be reached (Polat and Açikel, 2019).

Table 2: Kinetics modeling parameters of PFO, PSO and Elovich models for MB adsorption onto AR, Fe-P

Materials	Models	Parameters	5mg/L	10 mg/L	20 mg/L
AR	PFO	Q_{exp} (mg/g)	11.98	23.44	45.43
		Q_e (mg/g)	11.65	22.82	44.39
		K_1 (min^{-1})	0.250	0.223	0.221
		R^2	0.985	0.981	0.984
		Er	0.033	0.038	0.034
	PSO	Q_e (mg/g)	12.29	24.20	47.12
		K_2 (g/ mg x min)	0.040	0.017	0.008
		R^2	0.998	0.997	0.996
		Er	0.010	0.015	0.015
		Elovich	A	17063.35	7761.08
	B		1.188	0.539	0.269
	R^2		0.982	0.978	0.973
	Er		0.202	0.090	0.048
	Intra-particle diffusion		K_{int} (mg/g x $\text{min}^{1/2}$)	1.529	3.448
		C (mg/g)	7.079	13.860	26.001
R^2		0.822	0.804	0.779	
Er		0.040	0.048	0.055	
Fe-P	PFO	Q_{exp} (mg/g)	10.95	21.08	40.64
		Q_e (mg/g)	10.82	21.02	40.36
		K_1 (min^{-1})	0.451	0.368	0.344
		R^2	0.997	0.999	0.998
		Er	0.011	0.006	0.006
	PSO	Q_e (mg/g)	11.04	21.56	41.53
		K_2 (g/mg x min)	0.040	0.017	0.008
		R^2	0.998	0.997	0.996
		Er	0.008	0.012	0.014
	Elovich	A	40592.6	46001	26808.4
		B	3.802	1.486	0.684
		R^2	0.998	0.988	0.985
		Er	0.459	0.471	0.210
		Intra-particle diffusion	K_{int} (mg/g x $\text{min}^{1/2}$)	0.407	1.209
	C (mg/g)		9.787	18.028	34.145
R^2	0.926		0.858	0.831	
Er	0.019		0.028	0.033	

Modeling Adsorption Isotherms Parameters

To accurately describe the experimental equilibrium adsorption data, four models were employed: Langmuir, Freundlich, Redlich-Peterson, and Langmuir-Freundlich (Fig. 14).

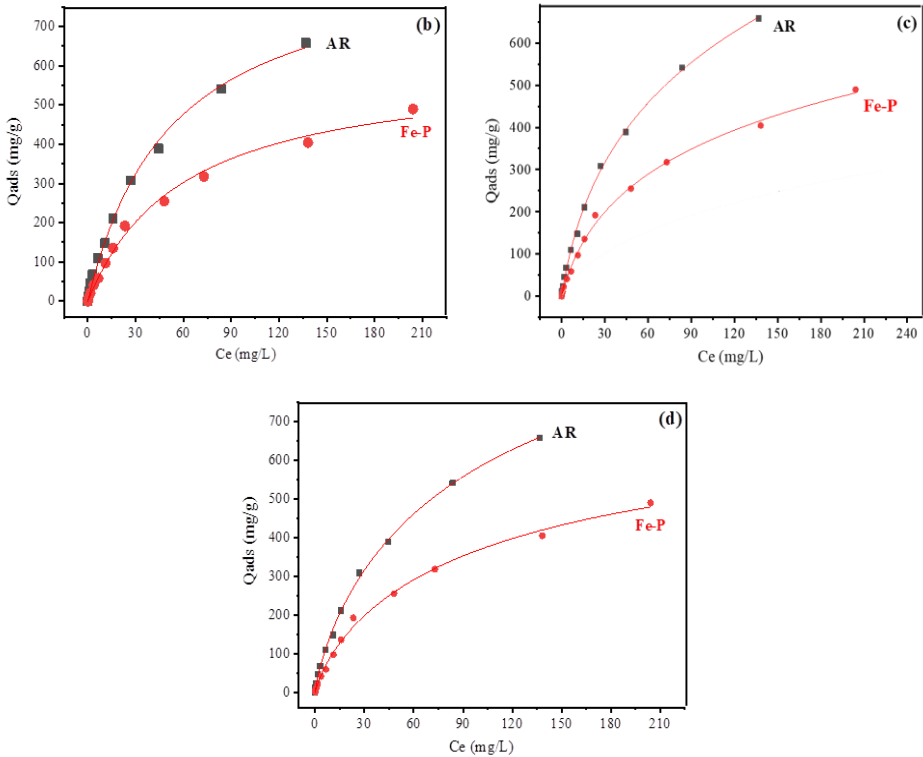


Figure 14: The Freundlich (a); Langmuir (b); Redlich-Peterson (c); and Langmuir-Freundlich (d); models were applied to fit the equilibrium adsorption isotherms of AR, and Fe-P onto MB, at a temperature of 20°C

Fig. 15 presents the Langmuir model, with two parameters (K_L and Q_{max}), assumes monolayer and homogeneous adsorption without molecular interactions (Langmuir, 1918). In contrast, the Freundlich model, also with two parameters (n and K_F), posits multilayer and heterogeneous adsorption with intermolecular interactions. The value of $1/n$ indicates adsorption intensity or surface heterogeneity; as it approaches zero, diversity increases, while adsorption is favorable when $1/n$ is less than 1 (Freundlich, 1907). The Redlich-Peterson model combines Langmuir and Freundlich approaches using three parameters (K , α , and β), suitable for describing adsorption equilibrium at high adsorbate concentrations (Ho et al., 2002; Tran et al., 2017). Lastly, the Langmuir-Freundlich model, with three parameters (Q_S , b , and n), behaves like a Freundlich isotherm at low adsorbate concentrations and predicts

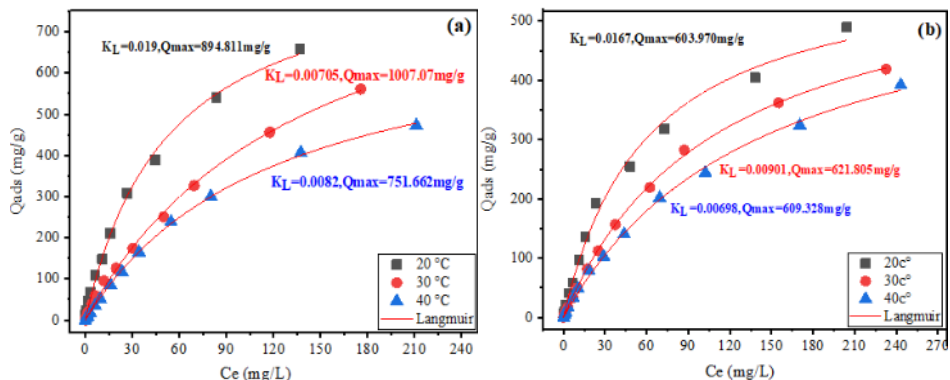


Figure 15: Experimental data points for AR (a), and Fe-P (b) at various temperatures were fitted using the nonlinear Langmuir isotherm model

Monolayer adsorption capacity similar to the Langmuir isotherm at high concentrations (Ho et al., 2002). The equilibrium data analysis in Table 3 reveals that all models exhibited a good fit with R^2 values of 0.99. The Langmuir isotherm emerged as the best-fitting model, with R^2 values of 0.997, 0.995 for AR, and Fe-P, respectively. The model yielded maximum adsorption capacities of 894.81 mg/g, 603.96 mg/g for AR, and Fe-P, respectively.

Table 3: Parameters of Adsorption Isotherms models on AR, and Fe-P

Models	Materials	Parameters				
Freundlich	AR	K_f (mg/g)/(mg/L) ^{1/n}	n	R^2	E_r	
						45.580
Langmuir	Fe-P	K_L (L/mg)	Q_{max} (mg/g)	R^2	E_r	
						31.519
Langmuir	Fe-P	K_L (L/mg)	Q_{max} (mg/g)	R^2	E_r	
						0.0189
Redlich-Peterson	Fe-P	K (L/g)	α (mg/L) ^{-β}	β	R^2	E_r
Redlich-Peterson	Fe-P	K (L/g)	α (mg/L) ^{-β}	β	R^2	E_r
Langmuir-Freundlich	Fe-P	K (L/g)	α (mg/L) ^{-β}	β	R^2	E_r
Langmuir-Freundlich	Fe-P	Q_s (mg/g)	b	n	R^2	E_r
Langmuir-Freundlich	Fe-P	Q_s (mg/g)	b	n	R^2	E_r

Thermodynamic study of adsorption

The determination of thermodynamic parameters ΔG , ΔH , and ΔS is essential for understanding and confirming the adsorption mechanism of MB on AR, and Fe-P. The change in Gibbs free energy ΔG indicates the spontaneity of adsorption under standard conditions. A negative ΔG ($\Delta G < 0$) signifies favorable and spontaneous adsorption; while

a positive ΔG suggests the process is not spontaneous (Anastopoulos et al., 2016). The standard enthalpy change ΔH reveals whether the process is endothermic or exothermic. Endothermic adsorption occurs when $\Delta H > 0$, while exothermic adsorption occurs when $\Delta H < 0$. The standard entropy change ΔS reflects the randomness at the adsorbate-adsorbent interface. When $\Delta S < 0$, the adsorption mechanism is associative and less random. Conversely, when $\Delta S > 0$, the process is more random and dissociative (Tran et al., 2016). The following equation relates these three thermodynamic parameters:

$$\Delta G = \Delta H - T\Delta S \tag{13}$$

$$\Delta G = -RT \ln(K_C) \tag{14}$$

$$\ln(K_C) = -\frac{\Delta H}{R} \times \frac{1}{T} + \frac{\Delta S}{R} \tag{15}$$

Gibbs's free energy change ΔG was determined using Eq. (13), while the change in enthalpy ΔH and change in entropy ΔS were derived from a plotting of $\ln(K_C)$ against $\frac{1}{T}$. The dimensionless equilibrium constant K_C was calculated by multiplying the Langmuir isotherm constant K_L by 55.5×10^3 and the molar mass of the adsorbate $M_{MB} = 320$ g/mol. This approach, represented by Eq. (16), has been utilized by various researchers (Anastopoulos et al., 2016; Ghosal et al., 2017), with T denoting absolute temperature and R ($8.314 \frac{J}{mol \cdot K}$) representing the universal gas constant.

$$K_C = K_L \times M_{adsorbate} \times 55.5 \times 10^3 \tag{16}$$

Thermodynamic analysis reveals an exothermic MB adsorption mechanism on AR, and Fe-P, as negative ΔH values indicate, favoring lower temperatures Table 4. The negative ΔS suggests decreased disorder at the solid-solution interface, while negative ΔG values confirm process spontaneity and favorability. ΔG magnitudes serve to differentiate between physical adsorption and chemisorption, with values above (20 KJ.mol⁻¹) typically indicating chemisorption. The observed decrease in adsorption capacity likely results from weakened hydrogen bonds or biosorbent degradation (Anastopoulos et al., 2016).

Table 4: Thermodynamics parameters of MB adsorption on AR, Fe-P

Adsorbent	T (°K)	ΔG° (KJ.mol ⁻¹)	ΔH° (KJ.mol ⁻¹)	ΔS° (J.mol ⁻¹ .K ⁻¹)
AR	293	-31.0082	-32.136	- 5.358
	303	-30.963		
	313	-29.569		
Fe-P	293	-30.701	-33.510	-10.037
	303	-30. 519		
	313	-30.187		

Regeneration of AR

The ability to regenerate adsorbents offers both economic advantages and practical necessity for sustainable operation. (Fig. 16) illustrates the reuse and regeneration performance of AR. The experimental results demonstrate that the adsorbent's efficiency gradually decreased over 7 consecutive cycles, with removal rates declining from 85.56% in the first cycle to 39.72% in the seventh cycle. This performance deterioration can be attributed to the progressive accumulation of MB molecules occupying the active sites on the AR surface. However, treatment with 0.1 M HCl effectively regenerated the adsorbent by promoting MB desorption and restoring the availability of active sites. These regeneration capabilities, combined with multiple reuse cycles, establish AR as a cost-effective and sustainable solution for MB removal from aqueous solutions.

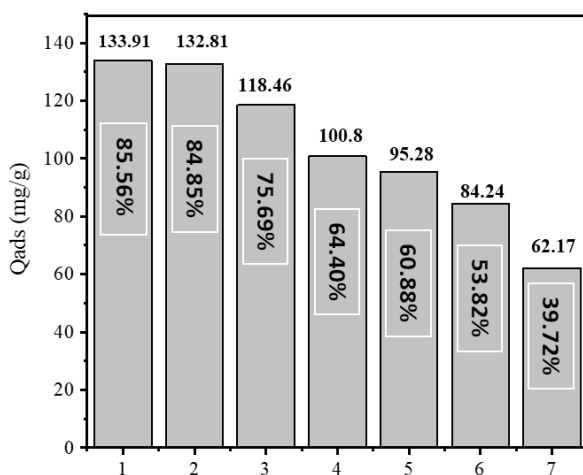


Figure 16: Regeneration of AR

CONCLUSION

This study demonstrates the effective use of rosemary-derived adsorbents for the removal of methylene blue (MB) dye from wastewater, offering sustainable and cost-effective solutions to industrial dye pollution. The activated rosemary carbon (AR) and iron-polyphenol nanoparticles (Fe-P) synthesized in this work exhibited distinct adsorption properties influenced by their structural and chemical characteristics. AR, with its highly porous and amorphous structure, achieved a superior maximum adsorption capacity of 894.81 mg/g, while Fe-P, characterized by its crystalline nanoparticle structure, exhibited faster adsorption kinetics and effective performance in acidic conditions. The adsorption processes for both materials were spontaneous and exothermic, as confirmed by thermodynamic analyses, with pseudo-second-order kinetics indicating surface adsorption as the primary mechanism.

Declaration of competing interest

The authors declare that they have no known competing financial interests or personal relationships that could have appeared to influence the work reported in this paper.

REFERENCES

- ABBA P., PENGOU M., BALKISSOU S., BADJOUKOUN Y., DELSIA L.J. (2019). Removal of purple of bromocresol from aqueous solutions by biosorption on a tropical biomass: the *Triplochiton Scleroxylon* (Ayus) saw, *Larhyss Journal*, No 39, pp. 59-76. (In French)
- AFROZE S., SEN T.K. (2018). A review on heavy metal ions and dye adsorption from water by agricultural solid waste adsorbents, *Water, Air, Soil Pollution*, Vol. 229, pp. 1-50.
- AICHOOR A., ZAGHOUANE B.H., CESAR V.S., SANCHEZ M.P. (2018). Bioadsorbent beads prepared from activated biomass/alginate for enhanced removal of cationic dye from water medium: Kinetics, equilibrium and thermodynamic studies, *Journal of Molecular Liquids*, Vol. 256, pp. 533-540.
- AL-GHOUTI M.A., KHRAISHEH M.A.M., AHMAD M.N.M., ALLEN S. (2009). Adsorption behaviour of methylene blue onto Jordanian diatomite: a kinetic study, *Journal of hazardous materials*, Vol. 165, Issues 1-3, pp. 589-598.
- ANANDAN K., RAJESH K., GAYATHRI K., MOHANBABU M., PRABHAKAR RAO P. (2023). Structural and photocatalytic properties of nickel oxide (NiO) and stannic oxide (SnO₂) nanoparticles synthesized via solvothermal process, *Larhyss Journal*, No 53, pp. 7-19.
- ANASTOPOULOS I., KYZAS G.Z. (2016). Are the thermodynamic parameters correctly estimated in liquid-phase adsorption phenomena, *Journal of Molecular Liquids*, Vol. 218, pp. 174-185.
- AWANG NASRIZAL A.A., FARZANA W., SAAD I., BOLONG N. (2023). Carbonized coconut shell media applicability for stormwater pollution control, *Larhyss Journal*, No 54, pp. 43-52.
- BANERJEE S., CHATTOPADHYAYA M.C. (2017). Adsorption characteristics for the removal of a toxic dye, tartrazine from aqueous solutions by a low-cost agricultural by-product, *Arabian Journal of Chemistry*, Vol. 10, pp. S1629-S1638.
- BENZIZOUNE S., NASSALI H., SRHIRI A. (2004). Study of the kinetics of adsorption of phosphorus in solution on the sediments of the Fouarat lake in Morocco, *Larhyss Journal*, No 3, pp. 171-184. (In French)
- BOUCHEMAL F., ACHOOR S. (2007). Tyrosine adsorption tests on grained and powdered activated carbon, *Larhyss Journal*, No 6, pp. 81-89. (In French)

- BOUDAOU A., AD C., DJEDID M., GUERMIT M., BENALIA M. (2024). Removal of azo toxic dye from aqueous solutions using dry spearmint sprigs, *Larhyss Journal*, No 59, pp. 29-51.
- CHAUHAN S.S., DIKSHIT P.K.S. (2023). Cadmium metal scavenging capability of spent tea grains - an agricultural biomass waste as a low-cost adsorbent, *Larhyss Journal*, No 55, pp. 161-189.
- DIZGE N., AYDINER C., DEMIRBAS E., KOBYA M., KARA S. (2008). Adsorption of reactive dyes from aqueous solutions by fly ash: kinetic and equilibrium studies, *Journal of hazardous materials*, Vol. 150, Issue 3, pp. 737-746.
- DJILALI K., MAACHI R., TAHRAOUI H., AIT MESBAH Z., AMRANE A. (2024). Advancing thermal stability analysis of haloperidol: Integrative approaches and optimization strategies for enhanced pharmaceutical formulations, *Journal of Molecular Structure*, Vol. 1315, Paper ID 138870.
- FADHIL D.H., AL-HUSSIN A., YOUSIF E. (2019). Removal of methylene blue dye from water using eco-friendly waste product (Eggshell) as an adsorbent and using the optimum adsorption conditions with real water sample from Tigris River, *Al-Nahrain Journal of Science*, Vol. 22, Issue 1, pp. 9-14.
- FREUNDLICH H. (1907). On adsorption in solutions, *Journal of Physical Chemistry*, Vol. 57, Issue 1, pp. 385-470. (In German)
- GAOUAR Y.M., GAOUAR B.N. (2016). Best available technology assessment of three existing processes in waste water treatment field, *Larhyss Journal*, No 27, pp. 105-123.
- GUPTA V.K., KUMAR R., NAYAK A., SALEH T.A., BARAKAT M.A. (2013). Adsorptive removal of dyes from aqueous solution onto carbon nanotubes: a review, *Advances in colloid and interface science*, Vol. 193, pp. 24-34.
- GAN P.P., SHIHAN N.G., HUANG Y., YAU L.S.F. (2012). Green synthesis of gold nanoparticles using palm oil mill effluent (POME): a low-cost and eco-friendly viable approach, *Bioresource technology*, Vol. 113, pp. 132-135.
- GHOSAL P.S., GUPTA A.K. (2017). Determination of thermodynamic parameters from Langmuir isotherm constant-revisited, *Journal of Molecular Liquids*, Vol. 225, pp. 137-146.
- GUERGAZI S., AMIMEUR D., ACHOUR S. (2013). Elimination of humic substances of two Algerian surface waters by adsorption on activated carbon and bentonite, *Larhyss Journal*, No 13, pp. 125-137. (In French)
- HAMZEZADEH A., RASHTBARI Y., AFSHIN S., MOROVATI M., VOSOUGHI M. (2022). Application of low-cost material for adsorption of dye from aqueous solution, *International Journal of Environmental Analytical Chemistry*, Vol. 102, Issue 1, pp. 254-269.

- HAMEED K., SHAHUL M.P., SUNDARAM M.M. (2017). Adsorption of chromotrope dye onto activated carbons obtained from the seeds of various plants: equilibrium and kinetics studies, *Arabian Journal of Chemistry*, Vol. 10, pp. S2225-S2233.
- HO Y.S., PORTER J.F., MCKAY G. (2002). Equilibrium isotherm studies for the sorption of divalent metal ions onto peat: copper, nickel and lead single component systems, *Water, air, and soil pollution*, Vol. 141, pp. 1-33.
- KHELIEL O., OUAKOUBAK A.E.K., YUCEF L., ACHOUR S. (2015). Groundwater denitrification by adsorption on activated carbon and by coagulation-flocculation with aluminum sulfate, *Larhyss Journal*, No 21, pp. 191-200. (In French)
- KHELIFI O., MEHREZ I., BEN SALAH W., BEN SALAH F., YOUNSI M. (2016). Study of methylene blue (MB) adsorption from aqueous solutions on biosorbent prepared from Algerian datte stones, *Larhyss Journal*, No 28, pp. 135-148. (In French)
- KHELIFI O., MEHREZ I., YOUNSI M., NACEF M., AFFOUNE A.M. (2018). Methyl orange adsorption on biosorbent derived from mango seed kernels, *Larhyss Journal*, No 36, pp. 145-156. (In French)
- KHELILI H., ACHOUR S., REZEG A. (2010). Effectiveness of aluminum sulfate and activated carbon against aromatic organic pollutants, *Larhyss Journal*, No 9, pp. 99-110. (In French)
- KHELILI H., ACHOUR S., KONAN K.G., GUELLAL M. (2024). Kinetic and isotherm study of Methylene blue adsorption on orange peel activated carbon, *Larhyss Journal*, No 58, pp. 89-103.
- KNAPPE D.R.U. (2006). Chapter 9 - Surface chemistry effects in activated carbon adsorption of industrial pollutants, *Interface Science and Technology*, Vol. 10, pp. 155-177.
- KORDKANDI S.A., FOROUZESH M. (2014). Application of full factorial design for methylene blue dye removal using heat-activated persulfate oxidation, *Journal of the Taiwan Institute of Chemical Engineers*, Vol. 45, Issue 5, pp. 2597-2604.
- LANGMUIR I. (1918). The adsorption of gases on plane surfaces of glass, mica and platinum, *Journal of the American Chemical Society*, Vol. 40, Issue 9, pp. 1361-1403.
- MAGDY Y.H., ALTAHER H. (2018). Kinetic analysis of the adsorption of dyes from high strength wastewater on cement kiln dust, *Journal of Environmental Chemical Engineering*, Vol. 6, Issue 1, pp. 834-841.
- MASMOUDI T., GUERGAZI S., ACHOUR S. (2018). Mercury removal by activated carbon, *Larhyss Journal*, No 34, pp. 21-38. (In French)
- MUMTHAJ A.M.M., DISSANAYAKA D.M.S.H., MOWJOOD M.I.M. (2023). Enhancement of phosphorous removal from wastewater using Murunkan clay mixed media, *Larhyss Journal*, No 53, pp. 145-163.

- NARAYANAN K.B., SAKTHIVEL N. (2010). Biological synthesis of metal nanoparticles by microbes, *Advances in colloid and Interface Science*, Vol. 156, pp. 1-13.
- NAHIL M.A., WILLIAMS P.T. (2012). Pore characteristics of activated carbons from the phosphoric acid chemical activation of cotton stalks, *Biomass and bioenergy*, Vol. 37, pp. 142-149.
- NABOULSI A., NABOULSI I., REGTI A., EL HIMRI M., EL HADDAD M. (2023). The valorization of rosemary waste as a new biosorbent to eliminate the rhodamine B dye, *Microchemical Journal*, Vol. 191, Paper ID 108790.
- OUAKOUAK A.E.K., YUCEF L., ACHOUR S. (2010). Removal of atrazine by adsorption on powdered activated carbon, *Larhyss Journal*, No 9, pp. 121-129. (In French)
- OUAKOUAK A.K., YUCEF L. (2016). Adsorption of Cu²⁺ ions on powder activated carbon and a sodique bentonite, *Larhyss Journal*, No 27, pp. 39-61. (In French)
- OUNOKI S., ACHOUR S. (2014). Evaluation of the physicochemical and bacteriological quality of raw and purified wastewater from the city of Ouargla. Possibility of their recovery in irrigation, *Larhyss Journal*, No 20, pp. 247-258. (In French)
- PELEKANI C., SNOEYINK V.L. (1999). Competitive adsorption in natural water: Role of activated carbon pore size, *Water Research*, Vol. 33, pp. 1209–1219.
- POLAT G., AÇIKEL Y.S. (2019). Synthesis and characterization of magnetic halloysite–alginate beads for the removal of lead (II) ions from aqueous solutions, *Journal of Polymers and the Environment*, Vol. 27, pp. 1971-1987.
- RAVEENDRAN P., FU J., WALLEN S.L. (2003). Completely “green” synthesis and stabilization of metal nanoparticles, *Journal of the American Chemical Society*, Vol. 125, Issue 46, pp. 13940-13941.
- SHARMA H.S., ALI S.F., HUSSAIN S.M., SCHLAGER J.J., SHARMA A. (2009). Influence of engineered nanoparticles from metals on the blood-brain barrier permeability, cerebral blood flow, brain edema and neurotoxicity, An experimental study in the rat and mice using biochemical and morphological approaches, *Journal of nanoscience and nanotechnology*, Vol. 9, Issue 8, pp. 5055-5072.
- SHAH S., DASGUPTA S., CHAKRABORTY M., VADAKKEKARA R., HAJOORI M. (2014). Green synthesis of iron nanoparticles using plant extracts, *International Journal of Biological & Pharmaceutical Research*, Vol. 5, Issue 7, pp. 549-52.
- STANCIU M.C., NICHIFOR M. (2018). Influence of dextran hydrogel characteristics on adsorption capacity for anionic dyes, *Carbohydrate polymers*, Vol. 199, pp. 75-83.
- SARALA E., MADHUKARA N.M., VINUTH M., RAMI R.Y.V., SUJATHA H.R. (2020). Green synthesis of Lawsonia inermis-mediated zinc ferrite nanoparticles for magnetic studies and anticancer activity against breast cancer (MCF-7) cell lines, *Journal of Materials Science: Materials in Electronics*, Vol. 31, pp. 8589-8596.

- SHUKLA A., ZHANG Y.H., DUBEY P., MARGRAVE J.L., SHUKLA S.S. (2002). The role of sawdust in the removal of unwanted materials from water, *Journal of hazardous materials*, Vol. 95, Issues 1-2, pp. 137-152.
- SAHNOUN S., BOUTAHALA M. (2018). Adsorption removal of tartrazine by chitosan/polyaniline composite: kinetics and equilibrium studies, *International Journal of Biological Macromolecules*, Vol. 114, pp. 1345-1353.
- SONG E.X., ANURITA S., AAN M.N.A., TEO F.Y., WONG C.F. (2023). Performance of biochar in bioretention system for removal of mixed contaminant: A review, *Larhyss Journal*, No 54, pp. 123-143.
- TIWARI P., VISHWAKARMA M.C., JOSHI S.K. (2017). Adsorption of Pb (II), Cu (II), and Zn (II) Ions onto *Urtica dioica* leaves (UDL) as a low-cost adsorbent: Equilibrium and thermodynamic studies, *Modern Chemistry*, Vol. 5, pp. 11-18.
- TRAN H.N., YOU S.J., HOSSEINI-BANDEGHARAEI A., CHAO H.P. (2017). Mistakes and inconsistencies regarding adsorption of contaminants from aqueous solutions: a critical review, *Water research*, Vol. 120, pp. 88-116.
- TRAN H.N., YOU S.J., CHAO H.P. (2016). Thermodynamic parameters of cadmium adsorption onto orange peel calculated from various methods: A comparison study, *Journal of Environmental Chemical Engineering*, Vol. 4, Issue 3, pp. 2671-2682.
- WANG Z. (2013). Iron complex nanoparticles synthesized by eucalyptus leaves, *ACS Sustainable Chemistry & Engineering*, Vol. 1, Issue 12, pp. 1551-1554.
- WANG Z., FANG C., MALLAVARAPU M. (2015). Characterization of iron-polyphenol complex nanoparticles synthesized by Sage (*Salvia officinalis*) leaves, *Environmental Technology & Innovation*, Vol. 4, pp. 92-97.
- XIA C., SHI S.Q. (2016). Self-activation for activated carbon from biomass: theory and parameters, *Journal of Green Chemistry*, Issue 7.
- YADAV S., KHAN F., RATHORE K., VERMA S., MEHTA D. (2024). Household waste water treatment with the aid of activated charcoal, *Larhyss Journal*, No 60, pp. 133-150.
- YAGUB M.T., SEN T.K., AFROZE S., AFROZE S.S., ANG H.M. (2014). Dye and its removal from aqueous solution by adsorption: a review, *Advances in colloid and interface science*, Vol. 209, pp. 172-184.
- YEDDOU MEZENNER N., BENZAADI Z., LAGHA H. BENMAILI A. (2012). Study of the adsorption of a mixture of Bio-Calcitrating compounds in an aqueous medium, *Larhyss Journal*, No 11, pp. 7-16. (In French)
- YOUCEF L., OUAOUAK A., BOULANOUAR D., ACHOUR S. (2014). Study of the adsorbent power of powdered activated carbon for the elimination of phosphates from natural waters, *Larhyss Journal*, No 17, pp. 35-46. (In French)

- YUDHA S.P., TEKASAKUL S., PHOUNGTHONG K., PHOUNGTHONG K., CHUENCHOM L. (2019). Green synthesis of low-cost and eco-friendly adsorbent for dye and pharmaceutical adsorption: Kinetic, isotherm, thermodynamic and regeneration studies, *Materials Research Express*, Vol. 6, Issue 12, Paper ID 125526.
- ZHANG X., LIN S., CHEN Z., MEGHARAJ M., NAIDU R. (2011). Kaolinite-supported nanoscale zero-valent iron for removal of Pb_2^+ from aqueous solution: reactivity, characterization and mechanism, *Water Research*, Vol. 45, Issue 11, Paper ID 21529878.
- ZIELIŃSKI B., MIĄDLICKI P., PRZEPIÓRSKI J. (2022). Development of activated carbon for removal of pesticides from water: case study, *Science Reports*, Vol. 12, Article Number 20869.